Monthly Notices of the ROYAL ASTRONOMICAL SOCIETY

MNRAS **505,** 5896–5909 (2021) https://doi.org/10.1093/mnras/stab1639

Thermodynamic evolution of the $z = 1.75$ galaxy cluster IDCS J1426.5+3508

S. Andreon,[1]★ C. Romero,[2,3] F. Castagna,[1] A. Ragagnin,[4,5] M. Devlin,[3] S. Dicker,[3] B. Mason,[6] T. Mroczkowski,[7] C. Sarazin,[8] J. Sievers[9] and S. Stanchfield[3]

[1]*INAF–Osservatorio Astronomico di Brera, via Brera 28, I-20121 Milano, Italy*
[2]*Green Bank Observatory, 155 Observatory Road, Green Bank, WV 24944, USA*
[3]*Department of Physics and Astronomy, University of Pennsylvania, 209 South 33rd Street, Philadelphia, PA 19104, USA*
[4]*IFPU - Institute for Fundamental Physics of the Universe, Via Beirut 2, I-34014 Trieste, Italy*
[5]*INAF - Osservatorio Astronomico di Trieste, via G.B. Tiepolo 11, I-34143 Trieste, Italy*
[6]*National Radio Astronomy Observatory, 520 Edgemont Rd, Charlottesville, VA 22903, USAInsert Affiliation Text Here.*
[7]*European Southern Observatory, Karl-Schwarzshild-Str. 2, D-85748 Garching b. München, Germany*
[8]*Department of Astronomy, University of Virginia, P.O. Box 400325, Charlottesville, VA 22904, USA*
[9]*Department of Physics, McGill University, 3600 University Street, Montreal, QC H3A 2T8, Canada*

Accepted 2021 June 3. Received 2021 May 3; in original form 2020 October 8

ABSTRACT

We present resolved thermodynamic profiles out to 500 kpc, about r_{500}, of the $z = 1.75$ galaxy cluster IDCS J1426.5+3508 with 40 kpc resolution. Thanks to the combination of Sunyaev–Zel'dovich and X-ray data sets, IDCS J1426.5+3508 becomes the most distant cluster with resolved thermodynamic profiles. These are derived assuming a non-parametric pressure profile and a very flexible model for the electron density profile. The shape of the pressure profile is flatter than the universal pressure profile. The IDCS J1426.5+3508 temperature profile is increasing radially out to 500 kpc. To identify the possible future evolution of IDCS J1426.5+3508 , we compared it with its local descendants that numerical simulations show to be 0.65 ± 0.12 dex more massive. We found no evolution at 30 kpc, indicating a fine tuning between cooling and heating at small radii. At $30 < r < 300$ kpc, our observations show that entropy and heat must be deposited with little net gas transfer, while at 500 kpc the gas need to be replaced by a large amount of cold, lower entropy gas, consistent with theoretical expectation of a filamentary gas stream, which brings low entropy gas to 500 kpc and energy at even smaller radii. At $r \gtrsim 400$ kpc the polytropic index takes a low value, which indicates the presence of a large amount of non-thermal pressure. Our work also introduces a new definition of the evolutionary rate that uses unscaled radii, unscaled thermodynamic quantities, and different masses at different redshifts to compare ancestors and descendants. It has the advantage of separating cluster evolution, dependence on mass, pseudo-evolution, and returns a number with unique interpretation, unlike other definitions used in literature.

Key words: galaxies: clusters: general – galaxies: clusters: individual: IDCS J1426.5+3508 – galaxies: clusters: intracluster medium – X-rays: galaxies: clusters.

1 INTRODUCTION

Understanding the growth of large scale structure is one of the challenges of modern astrophysics. In massive clusters most baryons are in the intracluster medium (ICM; Vikhlinin et al. 2006; Andreon 2010 and references therein) and the ICM offers us the opportunity of determining the dynamical status of clusters, their formation and evolution (Voit 2005; Kravtsov & Borgani 2012) via the measurement of their thermodynamic profiles (electron density, temperature, pressure, and entropy). While these quantities can be measured with X-ray facilities such as the EPIC camera on XMM-Newton (Turner et al. 2001, Struder et al. 2001) and the ACIS on Chandra (Garmire et al. 2003), the observational cost dramatically increases with increasingly redshift. Consequently, the earliest evolutionary phases, e.g. at $z \sim 2$, are observationally poorly known (see our Section 3.1 for examples).

Instead, the Sunyaev–Zel'dovich (SZ; Sunyaev & Zel'dovich 1972) signal, a spectral distortion of the cosmic microwave background induced by inverse Compton scatter of electrons in the hot cluster gas, is largely redshift-independent, making the observational cost less redshift-dependent than it is in X-ray (e.g. Mroczkowski et al. 2019). However, to map the ICM beyond $z \approx 0.3$, a resolution of 10–20 arcsec is needed (20 arcsec correspond to 170 kpc at $z \approx 1$). Early interferometers (e.g. the SZA array[1]) did not resolve distant clusters, current interferometers lose the large spatial scales associated with the ICM emission (e.g. the Atacama Compact Array; Iguchi et al. 2009, see Di Mascolo et al. 2019, 2020). Large single-dish SZ telescopes, such as the *IRAM* 30m and the Green Bank telescope (*GBT*), coupled with multifeed receivers, are needed to

★ E-mail: stefano.andreon@brera.inaf.it

[1]http://www.mmarray.org/

sample spatial scales between 50 kpc and 700 kpc, and beyond, outside the local Universe, and also to identify, and later flag, point sources superimposed on the extended ICM emission. By measuring pressure, SZ instruments reduce the required X-ray exposures, as temperatures no longer need to be derived from X-ray spectra, which are observationally expensive. Combining SZ and X-ray data thus offers the possibility of studying the thermodynamic profiles of clusters at $z \sim 2$.

Only a dozen of $z \sim 1 - 1.4$ clusters, and only one beyond,[2] have resolved pressure profiles, and these shows a variety of shapes: while some are flatter than the universal pressure profile (Dicker et al. 2020, Ghirardini et al. 2021), others are consistent with it (Dicker et al. 2020; Ruppin et al. 2020) and similar to those of the local Universe (Ghirardini et al. 2021), suggestive of a possible evolution. We emphasize, however, that studied samples are far from being unbiased: first, clusters with non-universal pressure profiles exist even at low redshift (Andreon et al. 2019), and, second, pressure-selected clusters, such as SPT clusters studied by Ghirardini et al. (2021), favour clusters with high pressure by definition.

In this work, we compute the thermodynamic profiles for one of the most distant clusters with a resolved electron density profile, IDCS J1426.5+3508 at spectroscopic $z = 1.75$ (Stanford et al. 2012), combining deep *Chandra* data with MUSTANG-2 observations. By observing a very distant cluster, we maximize the redshift baseline for evolutionary studies and we probe earlier times. IDCS J1426.5+3508 was discovered in the near-infrared as a galaxy overdensity (Stanford et al. 2012). At a fixed mass, the galaxy overdensity is independent of the ICM, which is the focus of this paper.[3] This independence has the advantage that it guarantees that the measured quantity is not biased by the way the object is selected, unlike samples selected by pressure.

IDCS J1426.5+3508 was later targeted and detected with the low (2 arcmin) resolution Sunayev–Zel'dovich Array (Brodwin et al. 2012). Mass estimates from that work (Brodwin et al. 2012) involving the integrated SZ signal and deep *Chandra* data (Brodwin et al. 2016) scatter around a value of about $M_{500} \sim 2.5\,10^{14}$ $M_\odot$ ($r_{500} \sim 500$ kpc; all values are corrected to our adopted cosmology), making the cluster massive for its redshift.

Throughout this paper, we assume $\Omega_M = 0.3$, $\Omega_\Lambda = 0.7$, and $H_0 = 70$ km s^{-1} Mpc^{-1}. Results of stochastic computations are given in the form $x \pm y$, where x and y are the posterior mean and standard deviation. The latter also corresponds to 68 per cent uncertainties because we only summarize posteriors close to Gaussian in this way. All logarithms are in base 10.

2 OBSERVATIONS, DATA REDUCTION, AND ANALYSIS

2.1 SZ

The cluster has been observed with MUSTANG-2, a 215-element array of feedhorn-coupled TES bolometers (Dicker et al. 2014) at the 100m *GBT*. When coupled to the *GBT*, MUSTANG-2 has 10 arcsec full width at half-maximum resolution and an instantaneous field of view of 265 arcsec.

[2]SPT-CL0459-4947, that we later consider in this work, is at $z = 1.70-1.71$ (Mantz et al. 2020; Ghirardini et al. 2021), had an initial slightly larger photometric redshift, and its redshift was rounded up to $z = 1.9$ (McDonald et al. 2019; Ghirardini et al. 2021).

[3]ICM and galaxy are clearly correlated in the sense that more massive clusters have more of everything. However, selection effects act when the correlation is at fixed mass (e.g. Andreon & Bergé 2012).

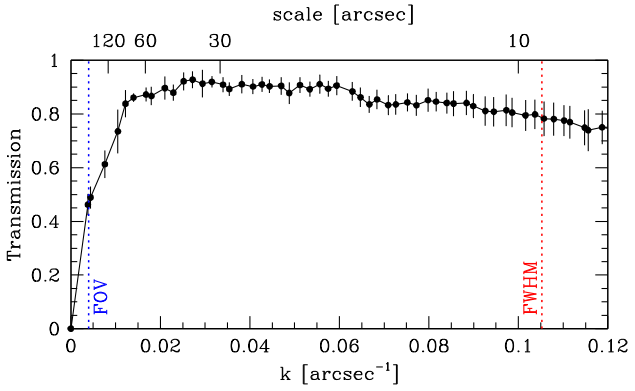

Figure 1. IDCS J1426.5+3508 MUSTANG-2 transfer function. Signal at scales smaller than 1.5 arcmin is, by large, preserved by the MIDAS data reduction but is increasingly reduced with increasing scales.

IDCS J1426.5+3508 was observed with Lissajous daisy scans, typically with a 2.5 arcmin radius. The cluster has been observed for a total on-source integration time of 5.0 h in 2018 April, June, and December. Data are calibrated using preferentially Solar systems objects, but also ALMA calibrators (Fomalont et al. 2014; van Kempen et al. 2014). Our SZ maps are calibrated to Rayleigh–Jeans brightness temperature (K_{RJ}); throughout this paper, brightness units of K are thus K_{RJ} unless otherwise noted. The final map has a RMS noise of 20 μK, when smoothed to the beam resolution, within the central 2 arcmin radius. A beam profile specific to this cluster observations is created by stacking all secondary (point source) calibrators used during these observations (see Ginsburg et al 2020).

Data are reduced following the traditional approach (named MIDAS in Romero et al. 2020, to which we refer for details): time ordered data from unresponsive detector or from bad scans and glitches are flagged, remaining ones are filtered to subtract atmospheric and electronic signal. This filtering also removes some (cluster) signal, which needs to be accounted for during the analysis using the transfer function, shown in Fig. 1. The transfer function is close to 0.8–0.9 up to scales of 1.5 arcmin, then drops to lower values for larger scales.

The resulting map is shown in Fig. 2. At a glance, the negative (SZ) signal has a pronounced elongation in the NW–SE direction; however, this is largely the effect of a bright (positive) source sitting 14 arcsec SW of the cluster, quite obvious in the map, that disappears in the point-source subtracted map. Because of the point-source brightness, we flagged and removed from further cluster analysis pixels inside a 20 arcsec diameter circle centred on the source. To account for the point source flux outside the aperture, we used the average beam measured from calibration observations interleaved with the cluster, regularized with a sum of two Gaussian, and scaled in intensity to match the point source. As a further precaution for pixels outside of the aperture the errors are boosted by 5 per cent of the subtracted flux to account for uncertainties in point source subtraction. This extra uncertainty has a minimal impact in the error budget. 5 per cent is a conservative estimate of the variation of individual beam observations. To compute the scaling factor of the beam to the point source, we fit the beam profile to pixels inside the aperture, assuming a constant level for the cluster plus background inside the small source aperture.

Fig. 3 shows the cluster radial surface brightness profile, extracted with 10″ radial annuli. Our forward model pressure profile, later fitted to these data, adopts the same radial bins, thus making the fitting

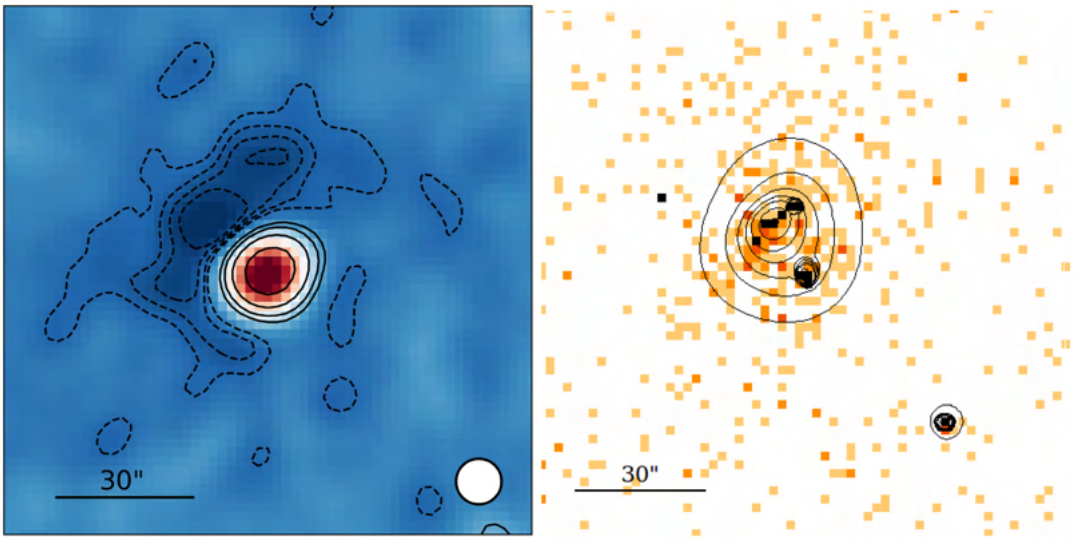

Figure 2. Multiwavelength view of IDCS J1426.5+3508 . Left-hand panel: MUSTANG-2 SZ map; negative contours start at -2σ, with 1σ steps. Positive contours start at 3σ and increment by a factor of 2. A bright point source is obvious at SW. The MUSTANG-2 beam is indicated in the bottom right. Right-hand panel: Adaptively smoothed *Chandra* [0.5–2] keV contours on the top of a binned [0.5–2] keV *Chandra* image. Three bright sources are obvious; the SW one at 14 arcsec from the cluster centre is also obvious in the SZ map.

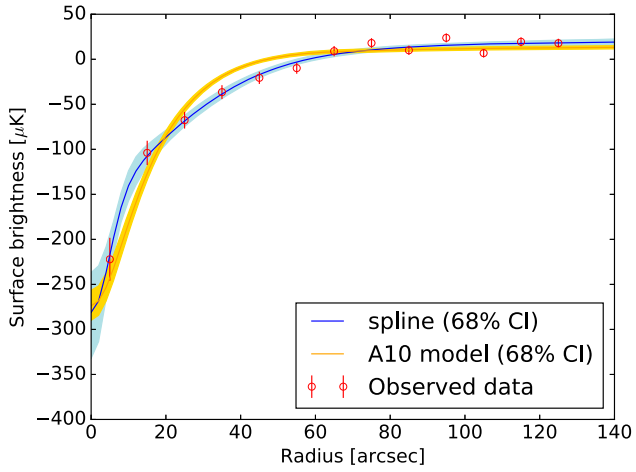

Figure 3. IDCS J1426.5+3508 surface brightness profile (points with error bars) and 68 per cent uncertainties on the fitted model. The adopted spline for the pressure profile is able to well describe the observed data, whereas a pressure profile with parameters fixed to A10 does not. In the latter case, model errors are meaningless.

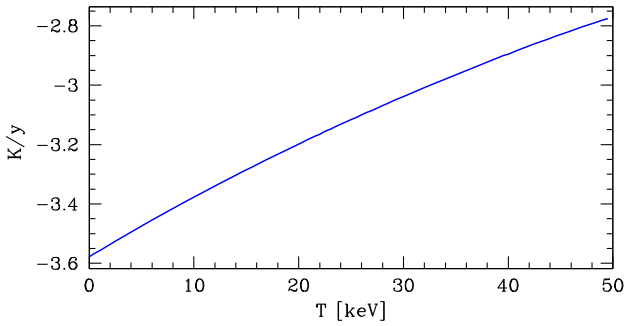

Figure 4. Cluster temperature dependence of the conversion from Compton y to Kelvin.

results independent of the adopted annular width. The profile levels off to $\approx 10\,\mu$K, and therefore our analysis requires one additional parameter, that we name the pedestal, to model this non-zero level. The non-zero pedestal originates from the data reduction, which forces the map to have zero mean.

The analysis of SZ data also requires the point spread function (PSF), measured on the beam image, and the conversion from K to Compton y, computed using relativistic corrections from Itoh et al. (2004) as shown in Fig. 4. The conversion is described by a second order polynomial, $-9.126\,10^{-5}T^2 + 0.02067T - 3.575$, with better than 0.1 per cent precision. The conversions between brightness temperature (K_{RJ}) and Compton y accounts for conversion to $K_{\rm CMB}$ and the bandpass for MUSTANG-2, which includes optical filters and Ruze efficiency of the primary dish on the *GBT*.

The three-dimensional pressure profile is derived fitting the SZ data with a modified version of `PreProFit` (Castagna & Andreon 2019), accounting for the transfer function, PSF, and pedestal level. Rather than fit the shape of the pressure profile to a pre-determined model [e.g. a generalized Navarro, Frenk, & White (1997) model with parameters fixed to the Arnaud et al. (2010) values], we allow the shape of the pressure profile to vary almost arbitrarily. However, for our subsequent analysis, we require a pressure profile that is continuous and doubly-differentiable. Thus, we fit the observed SZ data with a cubic spline in log-log space with knots at radii of r = 5, 15, 30, and 60 arcsec. Our model then has five variables: the pressures at these four points, P_0, P_1, P_2, and P_3, and the pedestal value of the SZ surface brightness. By defining the spline in log quantities (log pressure versus log radius), we naturally exclude non-physical (negative) values of pressure and radius and we can approximate a large variety of profiles, and their derivatives, including the commonly pressure profile parametrized as in Nagai et al. (2007). In our observational setting, the adopted choice is advantageous compared to the Nagai et al. (2007) parametrization because in the latter the degeneracy between pedestal parameter and the scale radius propagates to the three remaining parameters.

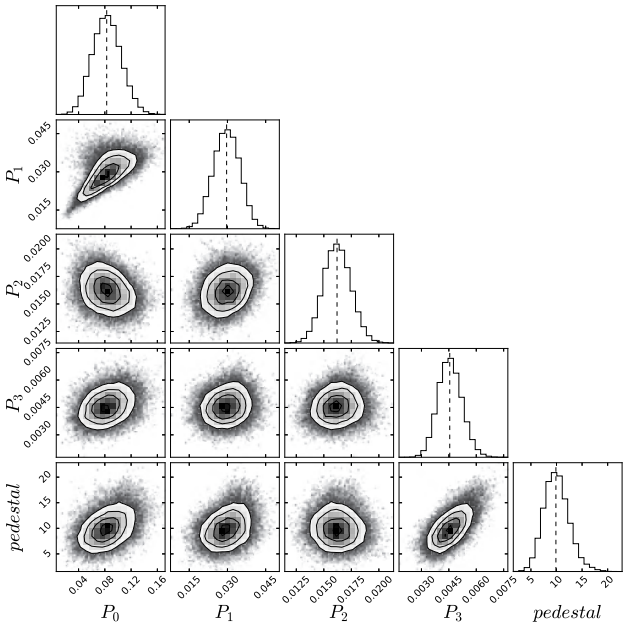

Figure 5. Joint and marginal probability contours for our SZ-only fit. Units: keV cm^{-3} for pressure parameters and μK for pedestal.

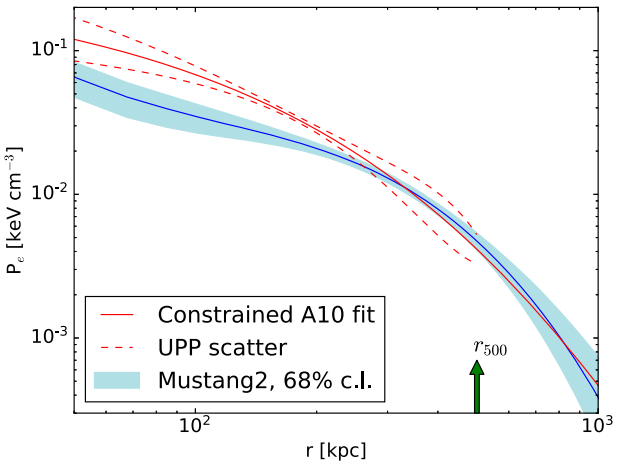

Figure 6. Observed MUSTANG-2 IDCS J1426.5+3508 pressure profile with 68 per cent uncertainties (solid curve and shading) versus a constrained universal profile fit to low resolution SZ interferometric data. Note that the displayed radial range includes radii poorly sampled by CARMA data ($r \ll 1$ arcmin, about 500 kpc), or MUSTANG-2 ($r \gtrsim 1$ arcmin). There is a good agreement on scale where interferometric data are most sensitive, and notable differences (25 per cent reduction) at smaller radii. The Arnaud et al. (2010) scatter around the universal profile is also indicated.

Prior to jointly fitting SZ and X-ray data (Section 2.3), we perform a SZ-only analysis that assumes spherical symmetry and $kT = 5$ keV. We also assume uniform priors, zeroed for unphysical values (e.g. pressure cannot be negative). In particular, since the total mass of the cluster is finite, the logarithmic slope of pressure should be steeper than -4 at large radii (Romero et al. 2018). We therefore adopted a logarithmic slope <-2 at $r = 1$ Mpc ($\sim 2r_{500}$) as prior. This prior could alternatively be expressed as a maximal value for the pedestal level. The imposition of this prior is primarily necessary due to the removal of cluster signal at these larger scales (the reduction itself is agnostic as to the true background level).

We find $P_i = 0.083 \pm 0.022$, 0.029 ± 0.005, 0.016 ± 0.001, 0.0045 ± 0.0006 keV cm^{-3}, and a pedestal level of 10 ± 3 μK with little covariance, illustrated in Fig. 5. We found a χ^2 of 12.0 for 8 degrees of freedom. Fig. 3 shows the best-fitting model, with the 68 per cent uncertainty, on top of the observed data. Fig. 6 shows the SZ-derived pressure profile as a blue line with 68 per cent uncertainty as the shaded area. This is the first $z > 1.45$ cluster (Dicker et al. 2020) with a resolved SZ-based pressure profile. The pressure profile is accurately determined out to r_{500} at least, where the cluster SZ brightness is 3σ away from the pedestal when measured in a narrow annulus $10''$ wide (i.e. discarding information at adjacent radii).

The fit adopts the X-ray centre (see next section), and accounts for a $\sim$4 arcsec astrometric offset with the *Chandra* image, the latter computed using the point source. The SZ centre is 5 arcsec away from the X-ray centre, in the direction of the point source, improving upon the 30 arcsec offset (and uncertainty) found on the old CARMA data. Fit results are robust to the limiting integration radius along the line of sight, taken to be 2.5 Mpc. We note that integration to larger radii, e.g. 5 Mpc, or smaller one, e.g. 1 Mpc, does not appreciably change the results.

Many previous SZ analyses of high redshift clusters lacked sufficient angular resolution to allow detailed pressure profiles to be derived. For example, CARMA observations of XLSS122 at $z_{\rm phot} \sim 1.9$ (Mantz et al. 2014, 2018), or of IDCS J1426.5+3508 itself by Brodwin et al. (2012) do not resolve the cluster and thus require a pressure profile shape be assumed. The same assumption is required for the analysis of many interferometric observations of clusters at lower redshift (e.g. the AMI Consortium et al. 2013; Brodwin et al. 2015; Rumsey et al. 2016) for the detection of *Planck* clusters (e.g. Planck Collaboration 2013), for estimating masses from ACT data (e.g. Hilton et al. 2018), and for analyses of interferometric observations only sampling the smallest scales, such as with the Atacama Compact Array (Di Mascolo et al. 2020). The resolved pressure profile of IDCS J1426.5+3508 allows us to test this common assumption on the profile shape at very high redshift. Fig. 6 compares the IDCS J1426.5+3508 pressure profile with the fitted profile from Brodwin et al. (2012). To fit their low (2 arcmin) resolution interferometric data, Brodwin et al. (2012) assume the universal pressure profile as determined by Arnaud et al. (2010; hereafter, A10) with the additional constraint that the cluster has to lay exactly (with no scatter) on the $Y_{500} - M_{500}$ relation of Andersson et al. (2010), yielding a fit with effectively one degree of freedom. There is a good agreement on arcminute scales (1 arcmin is $\approx$500 kpc) where CARMA interferometric data are most sensitive, and also notable differences (25 per cent reduction) at smaller radii, which are not sampled well by CARMA. This illustrates the value of high angular resolution SZ data, particularly if the field of view is sufficiently large to cover the entire cluster. Fig. 3 quantifies the amplitude of the discrepancy by fitting the surface brightness profile with one free parameter, as done in many papers (plus free pedestal, requested by our data). More precisely, we hold r_p to 500 kpc and the other parameters to the Arnaud et al. (2010) value. This profile is clearly rejected by our data ($\chi^2 = 36.4$ for 11 degree of freedom). Some other clusters at lower redshift, $z_{\rm med} = 1.2$, show deviations from the universal pressure profile as those we observe for IDCS J1426.5+3508, either a lower central pressure or an excess at large radii (Dicker et al. 2020). In the local Universe, the cluster CL2015 (Andreon et al. 2019) shows an even more remarkable flat pressure profile, a factor of 3 underpressured compared to the universal profile in the inner 500 kpc.

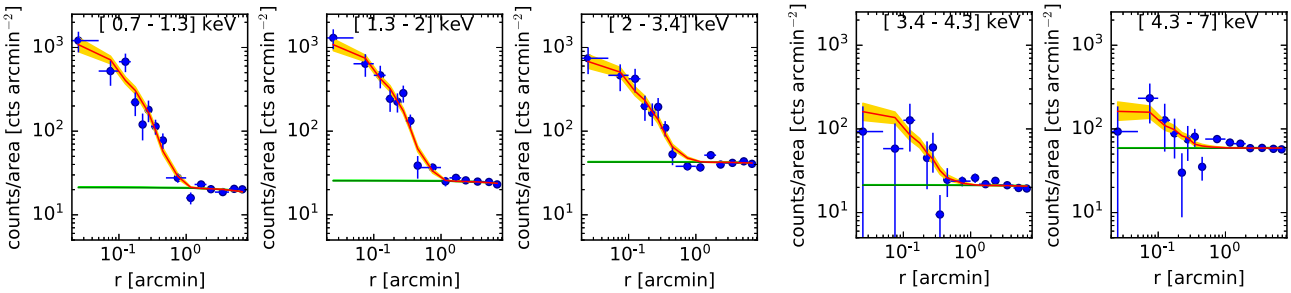

Figure 7. IDCS J1426.5+3508 surface brightness profile (points with error bars) in the X-ray bands, after coadding the two pointings and adjacent energy bands, with 68 per cent uncertainties on the fitted model (red line and yellow shading). The green line with lime shading (barely visible) is the background radial profile and its 68 per cent uncertainty. The analysis uses Poisson errors, separated pointings, and bands, not the plotted values and errorbars. The assumed X-ray cluster model (red line) captures the observed X-ray profiles at all energies.

The mismatch between IDCS J1426.5+3508 and the universal pressure profile is perhaps negligible for the derivation of the integrated Comptonization based on observations sampling large scales, because the integral is dominated by the signal at large radii.[4] However, the mismatch becomes crucial when the shortest spatial scales are used to recover the signal at larger scales, as already noted by Di Mascolo et al. (2020) for Atacama Compact Array observations. This highlights the importance of sampling both small and large spatial scales: Di Mascolo et al. (2020) hypothesize departures from the universal pressure profile to explain differences between integrated pressures measured with CARMA and Atacama Compact Array. Hilton et al. (2018) make the same hypothesis to explain the difference between masses (actually, integrated pressure) estimated from *Planck* and ACT, which are sensitive to different spatial scales. This work (Figs 6 and 3) and Dicker et al. (2020) show these departures thanks to a resolved pressure profiles measured with an instrument sensitive to both small and large scales. The nature of these departures are characterized below with complementary probes of the ICM, such as those accessible from X-ray observations.

2.2 X-ray

The *Chandra* ACIS-I X-ray data (obs ID 15168, 16321 with total exposure time of 100 ks; PI: Brodwin) were reduced following the standard procedures (e.g. Castagna & Andreon 2020). We briefly review the procedures here. We first removed background flares. Subsequently, we detect point sources using a wavelet detection algorithm and we masked them. Events (photons) are partitioned into 10 bands ([0.7–1.0], [1.0–1.3], [1.3–1.6], [1.6–2.0], [2.0–2.7], [2.7–3.4], [3.4–3.8], [3.8–4.3], [4.3–5.0], and [5.0–7.0] keV). To calculate the effective exposure time, we computed energy-dependent exposure maps accounting for vignetting, dithering, gaps, CCD defects, and flagged pixels. To measure the radial profiles, we then adopted circular annuli with an increasing width with radius to reduce the impact of the decreasing intensity of the cluster. The minimal width is taken to be 3 arcsec, larger than the *Chandra* PSF. We only considered annuli where the exposure time is larger than 50 per cent of the on-axis exposure time and included in the field of view by more than half of its area. The cluster centre is iteratively computed as the centroid of X-ray emission within the inner 20 kpc. The ancillary response and redistribution matrix files are derived using CIAO tools (with CALDB 4.8.3).

Proper background modelling is important for spectral analysis, especially in regions of low surface brightness. We use blank field images using CIAO BLANKSKY (Fruscione et al. 2006), normalized to the count rate in the hard band [9–13] keV to derive the background surface brightness in the 10 bands accounting for exposure time variations, dithering, vignetting, CCD defects, gaps, and flagged pixels. Background fields are mostly used to measure the spatial shape of the background in the various bands, or, equivalently, the spatial dependence of the background spectrum.[5] The background normalization is constrained in the fit by the counts in the cluster direction at large clustercentric distances.

Cluster observations are taken with two different orientations and pointings, and, as a consequence CCD gaps and sky coverage will differ between the two pointings. Furthermore, exposure time and background level differ between the pointings. These pointings are treated as independent data sets and are used jointly in our fits. In essence, we have four data cubes (two pointings, each with a cluster and a background cube) with 10 bins in energy and 15 radial bins, that we plot as radial profiles in different bands, shown in Fig. 7 (points and green line) after co-adding the two pointings and adjacent energy bands for illustrative purposes only. Each cube may also be alternatively seen as 10-point spectra taken at 15 different clustercentric distances.

There are 520 net photons within 4 arcmin of the cluster centre in the [0.7–7] keV band. Given the low number of net cluster photons over a 100 ks long background, faint morphological features, as surface brightness edges or cavities, cannot be detected. The X-ray peak is clearly displaced with respect to the brightest central galaxies by ≈15 kpc, as already remarked by Brodwin et al. (2016) using the very same data, indicative of a recent merger or gas sloshing.

In the X-ray only analysis of this section, SZ data are ignored and thermodynamic profiles were derived using MBPROJ2 (Sanders et al. 2018), a Bayesian forward-modeling projection code that fits the data cube accounting for the background. As with other approaches, MBPROJ2 makes the usual assumptions about cluster sphericity, clumping, and, when requested, hydrostatic equilibrium. However, it goes beyond the limitations of previous approaches, which apply arbitrary regularization kernels to deal with noise, ignore temperature gradients when deriving the electron density profile, or

[4]In the case of IDCS J1426.5+3508 , the spherically averaged dimensionless Comptonization within r_{500} is $7.0 \pm 0.5\,10^{-12}$ versus $7.9 \pm 3.2\,10^{-12}$ in Brodwin et al. (2012).

[5]The background has a spatial-dependent shape because it is formed by a vignetted and unvignetted part, and vignetting is energy-dependent.

ignore the spectral variation of the background, which represents the large majority of published papers, including previous X-ray analyses of IDCS J1426.5+3508 .

We fit the data twice to understand the impact of assumptions on the derived thermodynamic profiles. In the first descriptive analysis, we opted for an approach similar to Vikhlinin et al. (2006) and we modeled the temperature and electron density profiles with flexible functions constrained by the data. This is a fit aimed at simply describing the observations, with models introduced to impose regularity and smoothness. In particular, the `MBProj2` code models the electron density as a modified single-β profile following Vikhlinin et al. (2006):

$$n_e^2 = n_0^2 \frac{(r/r_c)^{-\alpha}}{\left(1 + r^2/r_c^2\right)^{3\beta-\alpha/2}} \frac{1}{\left(1 + r^\gamma/r_s^\gamma\right)^{\epsilon/\gamma}}. \quad (1)$$

Similarly to Vikhlinin et al. (2006), the temperature profile is given by the product of a broken power law with three slopes and a term introduced to model the temperature decline in the core region:

$$T = T_0 \frac{\left((r/r'_c)^{a_{cool}} + (T_{min}/T_0)\right)}{(1 + (r/r'_c)^{a_{cool}})} \frac{(r/r_t)^{-a}}{(1 + (r/r_t)^b)^{c/b}}. \quad (2)$$

The other thermodynamic profiles are derived from the ideal gas law. Following Vikhlinin et al. (2006), we fix $\gamma = 3$. As in some of Vikhlinin et al. (2006) fits, we adopt $\epsilon = 5$, and following Sanders et al. (2018) we use weak priors for the remaining six free electron density parameters. Following McDonald et al. (2014), we fix the inner slope to $a = 0$ and the shape parameter of the inner region to $a_{cool} = 2$, and we adopt weak priors for the remaining ones.

In the second fit, we adopt instead a physical model for the cluster: we assume a Navarro, Frenk, & White (1997, NFW) mass profile (for the dark matter only) and hydrostatic equilibrium, which makes explicit temperature profile modeling unnecessary. In this case, `MBProj2` computes the pressure profile given the NFW mass profile and derives the other thermodynamic profiles combining it with the electron density profile. As in our descriptive analysis, parameters are determined by fitting the data.

In both fits, metallicity is a free parameter, absorption was fixed at the Galactic N_H value in the direction of the cluster from Kalberla et al. (2005), and the results are marginalized over a further background scaling parameter to account for systematics (differences in background level between the cluster and control fields). The model is integrated on the same energy and radial bins as the observations, so that the results do not depend on the binning choice.

Fig. 7 illustrates how well the physical model (red line with 68 per cent uncertainty shaded) fit the data after co-addition and band-merging for illustrative purposes only. The fit uses instead the four data cubes.

All fit parameters show well-behaved posterior distributions with little or well-known covariances (e.g. $\beta - r_c$). The backscale parameter, which measures the amplitude of a potential (multiplicative) offset between the X-ray backgrounds in lines of sight of the cluster and background fields, is almost exactly one and extremely well determined, 1.006 ± 0.006. The gas metallicity is large, albeit with large errors: $Z_{Fe} = 0.8 \pm 0.5$ Solar. We verified that thermodynamic profiles are minimally affected by fixing metallicity at 0.3 Solar.

The electron density profile (upper panel of Fig. 8) is robustly determined and independent of the assumed model because it is primarily derived from the deprojected surface brightness profile that we can trace to 2 arcmin ($\sim$1 Mpc, $\approx 2r_{500}$).

Information on the X-ray temperature profile is encoded in the ratio of the cluster brightness in different energy bands, and temperature gradients are derived from radial variations in these ratios. X-ray data alone poorly constrain the IDCS J1426.5+3508 temperature profile (central panel of Fig. 8) and even less so its radial gradient. The X-ray based pressure profile shares limitations with the temperature profile because the pressure is derived from (the physical fit), or constrained by (the descriptive fit), the temperature. Indeed, the bottom panel of Fig. 8 shows the two X-ray derivations of pressure have large 68 per cent uncertainties that, furthermore, depend on the type of fit at $r > 200$ kpc (bars versus shading). At smaller radii, $r < 200$ kpc, the X-ray derived pressure has errors of ± 0.1 dex.

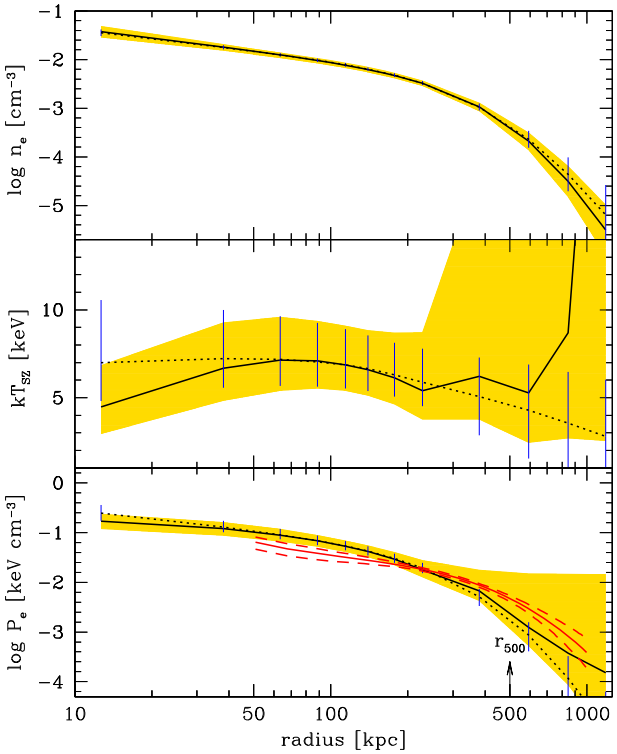

Figure 8. IDCS J1426.5+3508 electron density (top panel), temperature (middle panel), and pressure (bottom) profiles (mean value and 68 per cent uncertainties) from the X-ray only analysis (the physical fit is indicated by a solid line and yellow shading, while the descriptive fit by a dashed line and error bars; in the upper panel these are almost identical). The red solid line with the dashed corridor in the bottom panel indicates the results of the SZ analysis only (mean value and 68 per cent uncertainties). The SZ pressure profile is extrapolated beyond the outermost knot at $r \sim 500$ kpc.

In contrast, SZ data offer a more direct measurement of pressure and have typically negligible errors, $\sim$0.03 dex, at radii $r < 500$ kpc and are minimally affected by PSF at $r > 200$ kpc (Fig. 8, bottom panel, dashed lines). The constraints on thermodynamic profiles from X-rays extend to smaller radii because of the better resolution of Chandra compared to MUSTANG-2. X-ray and SZ pressure profiles are already consistent at about $\sim 2\sigma$ under the simplifying assumptions of this comparison: a perfectly known 5 keV isothermal cluster (assumed in the SZ-only analysis), perfect instrument calibrations, and identity between the gas-mass weighted (SZ) temperature T_{SZ} and the X-ray temperature T_X. Nevertheless, the SZ-derived pressure profile (solid red line) is flatter than X-ray-derived pressure profile (solid and dotted blue lines). Since the latter comes from a nearly constant temperature (yet very uncertain), the flatter SZ-derived pressure profile implies that the more precisely determined temperature profile derived combining the SZ-derived

pressure profile and X-ray derived electron density will be radially increasing, as quantified in the next section.

2.3 SZ+X-ray analysis

We now combine the SZ and X-ray data to make a fully joint fit, in which, for example the radial-dependent SZ conversion is estimated at a temperature given by, and therefore consistent with, the ratio of pressure and electron density profiles. We model the profile of electron density with the Vikhlinin et al. (2006) model (equation 1), and the profile of pressure with a cubic spline, adding to our previous analyses: (i) one more parameter to account for a possible SZ calibration systematics (a prior with $\sigma = 10$ per cent centred on 1.00; Romero et al. 2020; Dicker et al. 2020); (ii) we require consistency between the derived temperature profile and the temperature assumed in the SZ conversion coefficient used to derive it; and (iii) we allow the ratio between the X-ray and SZ temperatures to differ from 1 to account for *Chandra* temperature systematics (e.g. Schellenberger et al. 2015). In the fit, we do not assume hydrostatic equilibrium because of the likely radially increasing temperature profile that hints at the presence of possible disturbances.

The fit is performed with an updated version of JOXSZ (Castagna & Andreon 2020) that properly combines the SZ and X-ray analysis above. Our fitting model has four nuisance parameters, over which we marginalize, to account for data systematics: the backscale, to allow the X-ray background to deviate from the average in the cluster line of sight, the pedestal, to compensate for the forced zero-mean SZ map, the uncertainty on the SZ calibration, plus the parameter on the ratio of X-ray and SZ temperature to allow both *Chandra* calibration systematics and intrinsic differences between these two quantities. Furthermore, our analysis also uses the exact expression of the likelihood, which is a Poisson mixture model for the X-ray data (see Andreon et al. 2008; Castagna & Andreon 2020). Finally, since our fitting model is a fully forward one, all uncertainties are propagated to all quantities, for example the uncertainty on the T profiles induces an uncertainty on the X-ray and SZ conversion factors (which are in passing radial-dependent) propagated to the derived T profile and the other thermodynamic quantities.

The model fits the data quite well, in an indistinguishable way from what is shown for the two separate fits in Figs 3 and 7. All parameters show well-behaved posterior distributions with little or well-known covariances (Fig. 9). The relative calibration is very close to 1, 0.95 ± 0.10 (uncertainty is determined by the prior), the four P_i values, 0.093 ± 0.022, 0.037 ± 0.005, 0.017 ± 0.002, 0.005 ± 0.001 keV cm^{-3}, and pedestal, 13 ± 3 μK are consistent with those found in SZ-only fit. As in the X-ray only analysis, the backscale continues to be extremely close to 1 (1.007 ± 0.007) and metallicity is large although with large errors, $Z_{\rm Fe} = 0.8 \pm 0.5$ Solar. The X-ray temperature turns out to be larger than the SZ temperature $\log(T_{\rm X}/T_{\rm SZ}) = 0.09 \pm 0.11$ because pressure from SZ data is a bit low compared to the X-ray derived one within 300 kpc (Fig. 8). Our posterior value is consistent with the known temperature calibration systematics of *Chandra* (e.g. Schellenberger et al. 2015). We verified that the electron density profile is largely independent of ϵ by running our code with a wide prior on ϵ.

Fig. 10 shows the derived thermodynamic profiles. As expected, the pressure determination improves significantly when SZ data are included (compared to Fig. 8), and consequently the temperature profile also has smaller uncertainties. Since, as mentioned, at large radii the SZ pressure profile is flatter than the electron density profile (Fig. 8) the temperature profile turns up, which is anticipated. Because of the outward increasing temperature profile, the entropy profile turns up, while in most clusters it has a slope equal or lower than expected from non-radiative simulations (black dashed line). The thermal polytropic index, $\Gamma_{\rm th} = {\rm dlog}\,P/{\rm dlog}\,\rho$, computed using the pressure derived above which is only sensitive to the thermal component, turns out to be about 1.2 ± 0.2 at 70 kpc to decrease to 0.47 ± 0.06 at $r \gtrsim 400$ kpc (Fig. 11). Numerical simulations (Borgani et al. 2004; Shaw et al. 2010) suggest that the polytropic index computed using the total gas pressure, not just the thermal component, is about 1.2. Assuming that the simulations are correct and that the total pressure follows an adiabatic index of 1.2, the lower observed values at large radii for the thermal component indicates an important non-thermal support, i.e. gas motion or turbulence.

The radially increasing temperature, or, equivalently, the presence of a larger pressure than for a constant temperature profile, is robustly determined and unavoidable. First, the electron density profile at larger radii cannot be made shallower: given that the total number of collected photons at a fixed radius is fixed, the only way to flatten the n_e profile is to decrease the background radial profile, leading to a large increase in the percentage of the net number of cluster photons at large radii. The background, however, is constrained by the observed value at large off-axis angles and by the shape measured in the control fields, so that the normalization of the template background radial profile has almost no freedom (the backscale parameter has less than 1 per cent uncertainty, as mentioned). Concerning pressure, the flux density out to 1 arcmin (≈500 kpc) is well determined (Fig. 3) and, as a consequence, there is little freedom to force the pressure profile to bend here or at smaller radii, not even applying a strong prior on its slope. Also, CARMA data (Brodwin et al. 2012) confirm the pressure value at these radii (Fig. 6). Since the pressure is well measured at ≈500 kpc, changing the outer radius in the Abel (line of sight) integration has a negligible effect on the recovered pressure profile within 500 kpc. Therefore, a radially increasing temperature profile is, given the SZ and X-ray data, inescapable.

An increasing temperature profile over a sizeable part of the cluster is an uncommon feature in clusters at much lower redshifts, but not a novelty; for example, Abell 2034 (Owers et al. 2014) and MACS0417.5-1154 (Botteon et al. 2018) present large outer regions hotter than the cluster centre and body, as is also true of PLCKG266.6-27.3 at $z = 1.0$ (Bartalucci et al. 2018). Again at low redshift, Abell 2390, which is a plausible descendant of IDCS J1426.5+3508 (sec. 3.2) also has a monotonically increasing temperature profile until r_{500} (Vikhlinin et al. 2006). Equivalently, RXJ1347-1145 (e.g. Kitayama et al. 2004, Mason et al. 2010), and MACS0744 (Korngut et al. 2011) present an SZ enhancement outside the core interpreted as a temperature increase. If anything, in IDCS J1426.5+3508 we observe the temperature gradient well into a more peripheral region than usually observed in nearby clusters, but this could be due to the difficulties of detecting a temperature gradient in the cluster faint outskirts with current X-ray facilities.

Current IDCS J1426.5+3508 SZ and X-ray data have insufficient depth to allow us to discern in two-dimensional maps tiny morphological features, such as brightness edges, discontinuities, or cavities. This leaves the interpretation of the increasing temperature profile open: for example, the temperature can be low at the centre because of possible cavities produced by bubbles of radio plasma emitted by a central active galactic nucleus (AGN), as proposed by Vikhlinin et al. (2006) to explain the raising temperature profile of Abell 2390. Or we may be faced with an extreme case of sloshing, such as in Abell 2142 and Perseus (Simionescu et al. 2012; Rossetti et al. 2013). The latter is also corroborated by the offset of the X-ray emission compared to the BCG location, likewise present in IDCS J1426.5+3508. Our paper shows that by joining X-ray and SZ data,

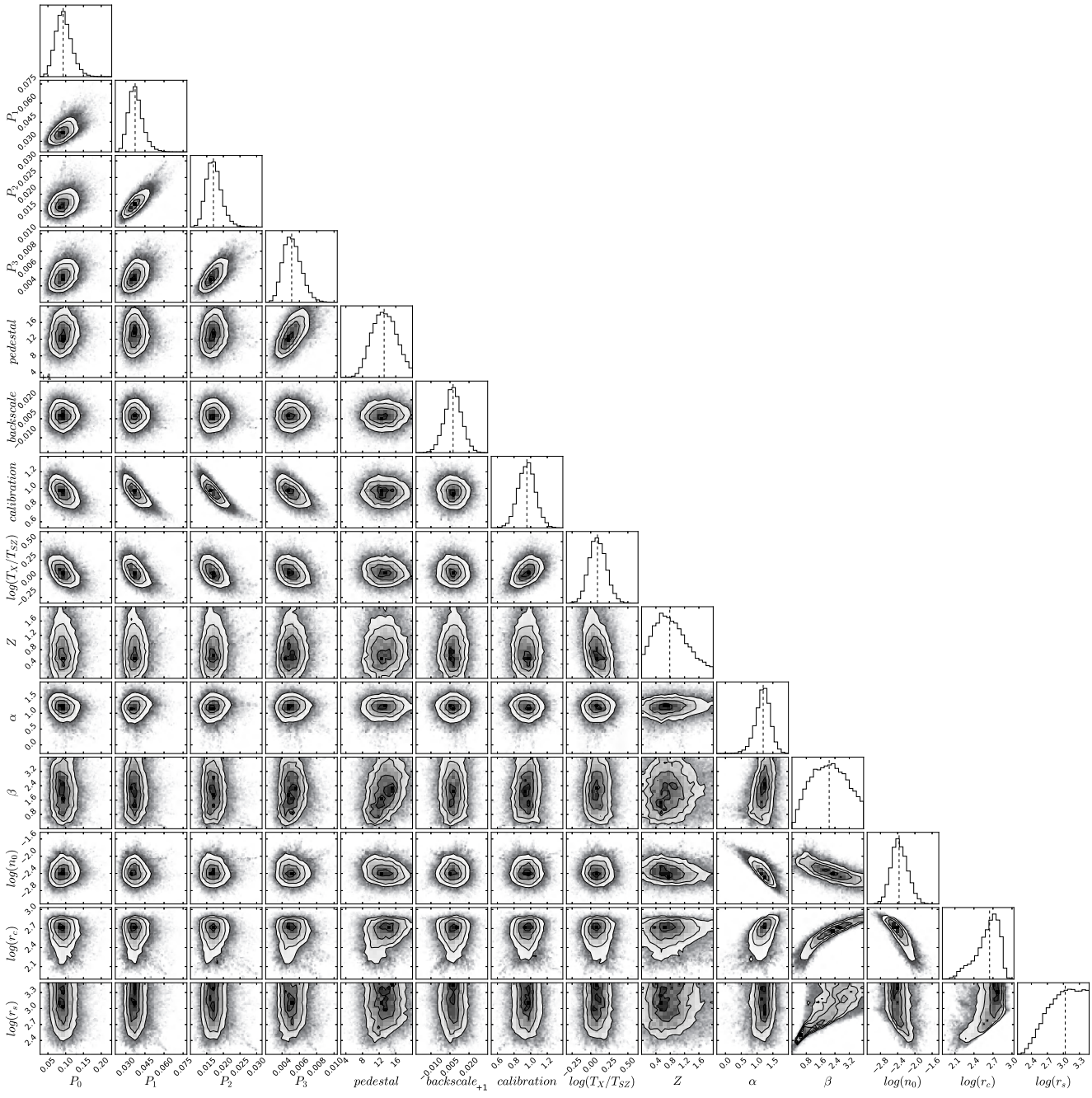

Figure 9. Joint and marginal probability contours for our X-ray + SZ fit. Units: keV cm^{-3} for pressure parameters, μK for pedestal, Solar for metallicity Z, cm^{-3} for density n_0, and kpc for radii. As detailed in the paper, uniform priors were taken for all parameters except the calibration, on the same scale (log when log are quoted). For the calibration, the Gaussian prior is very close to the marginal posterior.

no matter the precise interpretation, disturbances can be effectively detected via the different slopes of the electron density and pressure profiles (i.e. via SZ-based temperature profiles).

3 DISCUSSION

3.1 The efficiency of combining SZ and X-ray observations

Fig. 10 contrasts IDCS J1426.5+3508 profiles to those of a cluster at slightly lower redshift, SPT-CL0459-4947 at $z = 1.70$ (Ghirardini et al. 2021) derived by combining a longer *Chandra* exposure (170 versus 100 ks) and a exceptional XMM exposure on a high redshift cluster in place of a typical MUSTANG-2 observation (500 versus 18 ks).[6] Prior to our work, SPT-CL0459-4947 was the most distant cluster with well-resolved thermodynamic profiles. The uncertainty on density and temperature are comparable for the two clusters,

[6]Because of the lack of published covariance terms across parameters of a given profile and across thermodynamic quantities, plotted errors on SPT-CL0459-4947 only use the published diagonal terms. Note that the authors use base 10 log in plots, but we verified than many quantities quoted with log use instead Neperian (natural) log s.

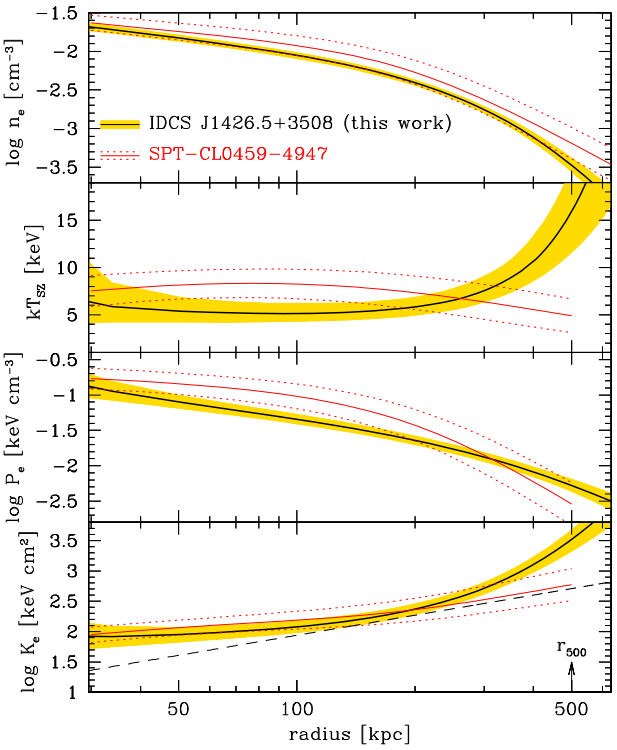

Figure 10. IDCS J1426.5+3508 thermodynamic profiles (mean value and 68 per cent uncertainties) from the X-ray + SZ analysis (black line and shading). To illustrate the quality of our determination, the thermodynamic profiles and approximated $\pm 1\sigma$ errors around the average of SPT-CL0459-4947 are also shown. SPT-CL0459-4947 is a slightly brighter and hotter cluster at slightly lower redshift, and its profiles are derived from a 70 per cent longer *Chandra* observations and 500 ks XMM in place of 18 ks MUSTANG-2. The dashed black line in the entropy panel is the Voit et al. (2005) fit to non-radiative simulations, as adapted by Pratt et al. (2010). The arrow indicates IDCS J1426.5+3508 r_{500}.

perhaps a bit smaller for IDCS J1426.5+3508 in spite of the handicap of its lower X-ray luminosity (lower n_e at all radii), while pressure is much better determined for IDCS J1426.5+3508. To summarize, when jointly fitting to a moderate X-ray exposure, a regular MUSTANG-2 observation compares well against exceptional X-ray allocations for the derivation of thermodynamic profiles. Furthermore, our *Chandra* plus MUSTANG-2 observations of IDCS J1426.5+3508 favourably compares in terms of precision to the Ghirardini et al. (2021) combination of 7 $z_{\rm med} = 1.4$ clusters, totaling over 2 Ms *Chandra* and XMM observations.

3.2 Evolution

IDCS J1426.5+3508 is one of the most massive clusters at high redshift (Brodwin et al. 2012). By selecting clusters of the same mass in the closest snapshot ($z = 1.71$) and their $z = 0$ descendants in Multidark Planck 2 simulation (Behroozi et al. 2013; Klypin et al. 2016), we find that by $z = 0$ the mass of IDCS J1426.5+3508 will plausibly have growth by 0.65 ± 0.12 dex. Therefore, we compare IDCS J1426.5+3508 with present-day 0.65 dex more massive clusters. We verified that the 0.12 dex scatter on the mass growth is largely subdominant for our conclusions compared to the variety of observed profiles at $z \sim 0$ at fixed mass. We use unscaled

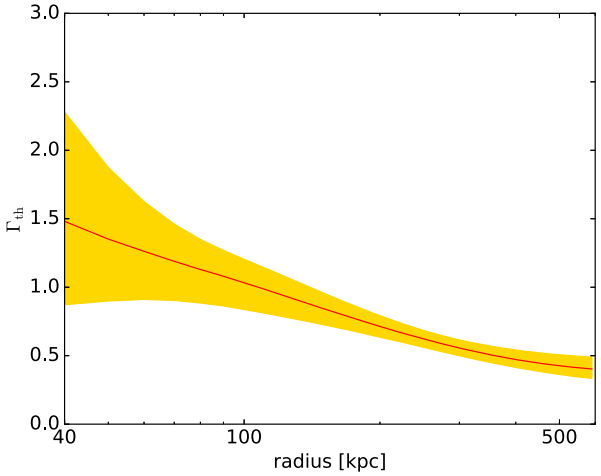

Figure 11. IDCS J1426.5+3508 thermal polytropic index profile Γ (mean value and 68 per cent uncertainties) from the X-ray + SZ analysis (black line and shading). The low value at large clustercentric distances indicate gas motion or turbulence.

radii and unscaled thermodynamic quantities (see Section 3.3 for discussion).

Fig. 12 compares the thermodynamic profiles of IDCS J1426.5+3508 with its $z = 0.07$ plausible descendants (solid red line, the corridor encloses $\pm 2\sigma$, based on X-COP; Ghirardini et al. 2019). Since X-COP clusters have lower masses than IDCS J1426.5+3508 descendants, their profiles are scaled up based on X-COP mass-dependent relations determined from a scaling measured at lower masses. To test this extrapolation, we also plot electron density, temperature, and entropy profiles (from Vikhlinin et al. 2006 and Sonkamble et al. 2015) of Abell 2390, whose mass matches the one IDCS J1426.5+3508 will have by $z = 0.23$ (the Abell 2390 redshift). Abell 2390 is well within the X-COP $\pm 2\sigma$ bounds, confirming the correctness of our extrapolation.

The comparison of IDCS J1426.5+3508 to its plausible descendant identifies three radial regimes showing different behaviours. At the very centre, $r = 30$ kpc, the gas had the same thermodynamic values 10 Gyr ago as today. If interpreted as AGN feedback regulating the inner cluster region (McDonald et al. 2017), this implies a fine tuning between AGN activity and gas cooling, to keep all four thermodynamic quantities close to constant with time in the last 10 Gyr.

Outside the centre and within 300 kpc, the gas amount in IDCS J1426.5+3508 is within the 2σ range of comparable low-redshift clusters. However, at about 500 kpc (about r_{500}), the electron density profile shows a drop and IDCS J1426.5+3508 is gas-poor relative to present-day descendants, which is understandable because descendants have accreted mass at large radii (see also Section 3.3). Within 300 kpc, the gas already present in IDCS J1426.5+3508 is colder and has lower entropy than in massive clusters at $z = 0$, while the opposite is true around 500 kpc. Therefore, to become a present-day cluster, heat and entropy must be transferred inwards from larger radii. At the same time a large gas deposit must occur at 500 kpc with little net gas transfer at smaller radii given the already appropriate electron density profile there. Therefore, outside the centre and within 300 kpc the emerging picture is one in which the gas of IDCS J1426.5+3508 is already present with the right amount but still far, in terms of temperature and entropy, from the properties of present-day clusters. Instead, the region at about 500 kpc was

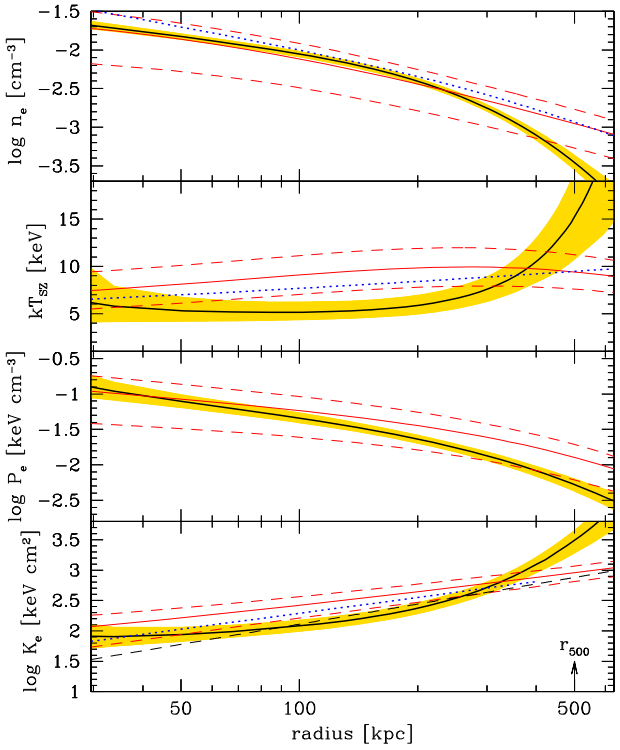

Figure 12. IDCS J1426.5+3508 (mean value and 68 per cent uncertainties, black line, and yellow shading) is compared to its present-day expected descendant (red line with dashed corridor mark the mean value and the $\pm 2\sigma$, based on X-COP). Compared to its present-day descendant, at large radii gas is lacking and that present is too hot and with large entropy. To become a present-day cluster, heat and entropy should be dissipated or the gas transported to larger radii plus cold and low entropy gas should be acquired from peripheral regions. In electron density, temperature and entropy panels the profiles of Abell 2390, a possible IDCS J1426.5+3508 descendant, are shown with dotted blue line. Abell 2390 lacks a published pressure profile measurement.

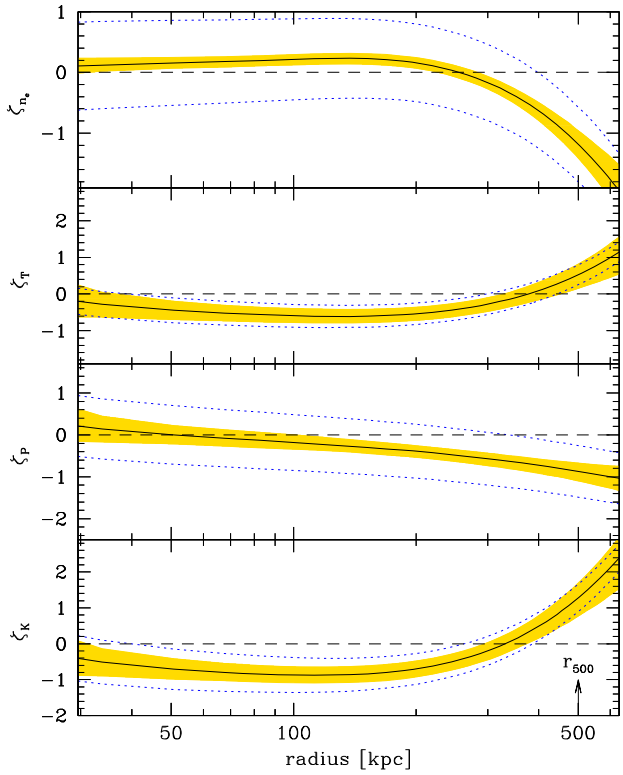

Figure 13. Evolutionary rates ζ measured at fixed progenitor. Redshift evolution (slope with $\log E(z)$) of the IDCS J1426.5+3508 thermodynamic profiles (mean value and 68 per cent uncertainties, black line and yellow shading) when compared to its present-day expected descendants. The dotted corridor marks three times the X-COP scatter about the average. Negative values indicate deficits in the past, while the no-evolutionary case correspond to $\zeta = 0$. The plot quantifies the evolutionary rates already appreciable in Fig. 12.

not yet developed 10 Gyr ago and the gas present there must either move away or evacuate the excess heat and entropy. The low thermal polytropic index supports this interpretation. This is theoretically feasible by a filamentary gas stream (Zinger et al. 2016), which can bring low entropy gas to r_{500} and bring energy into central regions that dissipates in form of heat, and shown from the hydrodynamic simulations in Section 3.3.

Fig. 13 quantifies the evolution of the thermodynamic profiles f by computing their evolutionary rates ζ. ζ is the power of the $E(z)^{\zeta}$ dependence,

$$f(r, z, M_z) = f(r, z = 0, M_{z=0})E(z)^{\zeta} \ , \qquad (3)$$

where $H(z) = H_0 E(z)$, and $M_{z=0}$ is the mass of the $z = 0$ plausible descendant of the cluster with mass M_z at redshift z. Clusters with different masses at different redshifts are considered in the attempt to emulate tracing a single cluster through time by comparing plausible ancestors and descendants (in the Section 3.4 we will consider different cases). Using log-quantities, ζ is given by the log difference between profiles at IDCS J1426.5+3508 redshift z and the reference profiles, divided by the baseline $\log E(z_{\rm IDCS}) - \log E(z_{\rm X-COP})$. A value of zero would therefore mean no $E(z)$ dependence at all. Fig. 13 shows the derived evolutionary rates and quantifies trends already appreciable in Fig. 12: in short, all thermodynamic quantities show almost no evolution at the centre; within ≈300 kpc, the density remains roughly constant, but heating and entropy increases are needed; at about 500 kpc, the density must increase while entropy and temperature decrease.

3.3 Interpretation of results

We use the Magneticum simulation (Hirschmann et al. 2015; Dolag et al. 2016; Ragagnin et al. 2017) to place our results in a broader context. The simulation self-consistently follows radiative cooling, star formation, black hole growth, metal enrichment, and associated feedback processes from both Type II/Ia supernovae and AGN. We consider the highest resolution with a 500 comoving Mpc^3 volume run (Hirschmann et al. 2015), the 22 most massive clusters at $z = 1.71$, and their $z = 0.07$ descendants. In spite of the simulation large volume and our choice of focusing on the most massive clusters, the considered haloes have similar, yet smaller, masses than IDCS J1426.5+3508 ($0.64 < M_{500}/10^{14}$ M$_\odot$ < 1.4 versus 2.5). Nevertheless, the selected haloes are adequate to highlight known theoretical behaviours, as detailed below. The mass M_{500} of the simulated clusters evolves by 0.60 ± 0.16 dex, and their r_{500} by a factor close to 3, which is close to what was found for more massive clusters in the baryon-free, large volume, Multidark simulation in Section 3.2.

Cluster growth is known to proceed in two phases: an early fast accretion, building the cluster central region largely not evolving at

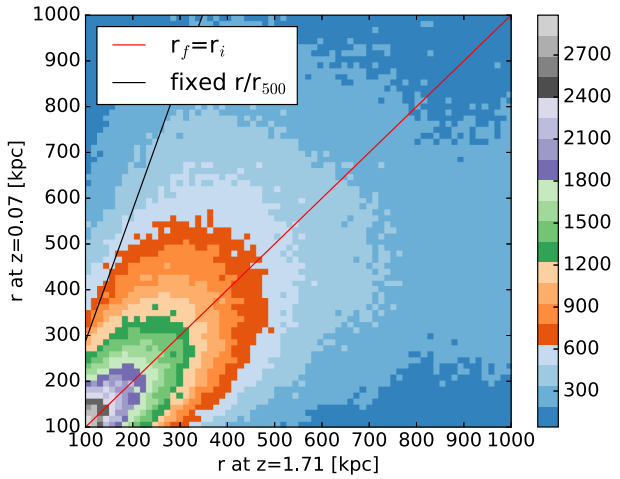

Figure 14. Two-dimensional histogram showing the distribution of $z = 0.07$ clustercentric distances (ordinate) of dark matter particles as a function of their clustercentric distances at $z = 1.71$ (abscissa) in massive clusters of the Magneticum simulation. When vertically read, this two-dimensional histogram plot indicates the present-day spatial distribution of the particles that were at distance indicated by their abscissa. The colour scale is proportional to their relative frequency. The locus of constant distance from the cluster centre is shown in red, whereas the black lines show the locus to be observed if particle distances grow as r_{500}, i.e. if r/r_{500} stays constant. Clearly, particles stay at similar distances from the cluster centre in the last 10 Gyr, far less than the factor of 3 increase experienced by r_{500}.

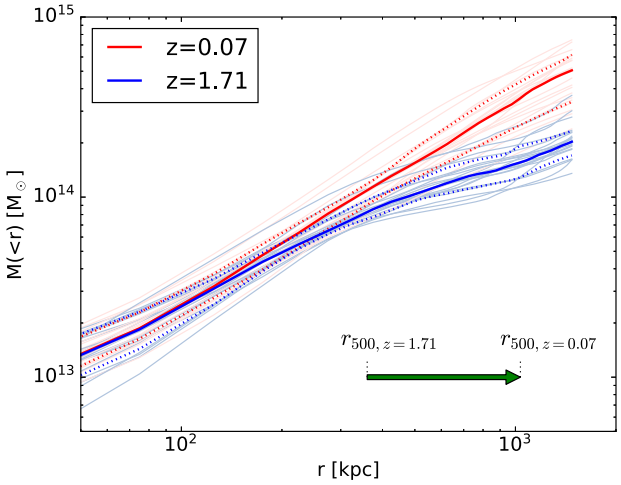

Figure 15. Cumulative mass of massive progenitors and their descendants in the Magneticum simulation. The solid line indicates the mean profile, the dotted corridor the 68 per cent range, individual profiles are plotted in light red or blue. While r_{500} increases, and by a sizeable amount in the considered redshift interval (shown by the arrow), clusters keep similar mass density profiles within $r_{500,z=1.71}$ while, at larger radii, particle distances decrease.

later times, and a later phase growing the less central part of the cluster (e.g. Gott & Rees 1975, Gunn 1977, and later works, e.g. Zhao et al. 2003, Lu et al. 2006). As nicely phrased by Böhringer et al. (2012), the Birkhoff theorem states that "the cluster evolution is not concerned with the background universe", clusters do not expand/contract in an expanding/contracting universe, or, to quote Peebles (1980) "a gravitational bound system such as the Local group is not expanding". Indeed, Fig. 14 shows that dark matter particles that were at $r < 500$ at high redshift are found at much the same radius at low z, as already known since Peebles (1980), in agreement with dark matter-only simulations in Zhao et al. (2003) and with the simple simulation in Lu et al. (2006). The figure also shows some more accretion from larger radii, in particular at $r \approx 1000$ (today) kpc, better visible in Fig. 15, illustrating the known accretion during the late phase, $z < 1.71$ in our case. While r_{500} *increases* by a factor of 3, mostly because it is anchored to the critical density (pseudo-evolution), radial distances of particles *decrease*, or stay constant within $r_{500,z=1.71}$, which is the only portion of the profile usually accessible at high redshift. Clusters do not expand, and this explains why we compare properties at unscaled (i.e. same) radii, which is highly appropriate for observed portion of IDCS J1426.5+3508 (within $r_{500,z=1.71}$), unlike many previous works (e.g. Bartalucci et al. 2017; McDonald et al. 2017; Ghirardini et al. 2021) that preferred instead to compare at fixed r/r_{500} (shown as black line in Fig. 14), i.e. consider larger clustercentric distances with decreasing redshift, while particle distances stay similar or change in the opposite direction.

Mostly because of the pseudo-evolution of r_{500}, the mass of the cluster increases, even in absence of any mass accretion. This implies that a comparison at fixed mass is not comparing ancestors and descendants, but 'unripe apples to ripe oranges in understanding how fruit ripens' (verbatim from Andreon & Ettori 1999). Therefore, our estimates of evolution are derived comparing ancestors and descendants (at evolving mass for IDCS J1426.5+3508), unlike some works discussed in the next section.

As mentioned, the Magneticum simulation has and follows gas particles. Fig. 16 shows the evolutionary rates ζ, derived for gas particles. At high redshift, clusters were denser (in gas density) in the centre (positive ζ_{n_e}) and smaller because the outer regions have not yet grown. They were also colder (negative ζ_T), and had a lower entropy (negative ζ_K). Since pressure is given by the product of electron density and temperature, its evolution is the sum (because of the use of log) of the evolution of the two quantities.

These trends are qualitatively similar to what is derived using real data (compare Fig. 16 with Fig. 13) and what we infer comparing high and low redshift clusters corresponds to what we observe following gas particles in the simulation: as we wrote for IDCS J1426.5+3508 in Section 3.2, the gas already present in the progenitor within about half $r_{500,z=1.71}$ is colder and has lower entropy than in the descendant and indeed heat and entropy is transferred inward, as we concluded for IDCS J1426.5+3508 . As found with the data, in the last 10 Gyr a large gas deposit occurs at $\approx r_{500,z=1.71}$, with low net gas transfer at much smaller radii (lower for IDCS J1426.5+3508 than for simulations). In Section 3.2 we argued that IDCS J1426.5+3508 gas at $\approx r_{500,z=1.71}$ must either move away or evacuate the excess heat and entropy, also supported by the low value of the polytropic index at $r \gtrsim r_{500,z=1.71}/2$. The bulk motion is obvious following the gas particles in the simulation, as the temperature and entropy change (Fig. 16). There are quantitative differences, however, between simulations and data: ζ amplitudes tend to be larger in simulation and at $r \gtrsim 500$ kpc, where the entropy IDCS J1426.5+3508 profile shape strongly deviates from the nearly constant behaviour seen in the simulated data. In particular, none of the individual simulated profiles matches, not even qualitatively, the large increase seen for IDCS J1426.5+3508. Larger volume simulations, or zoomed-in simulation of more massive clusters, are needed to understand if differences are due to (imprecise) assumptions on the simulation sub-grid physics or differences in the mass of the considered objects.

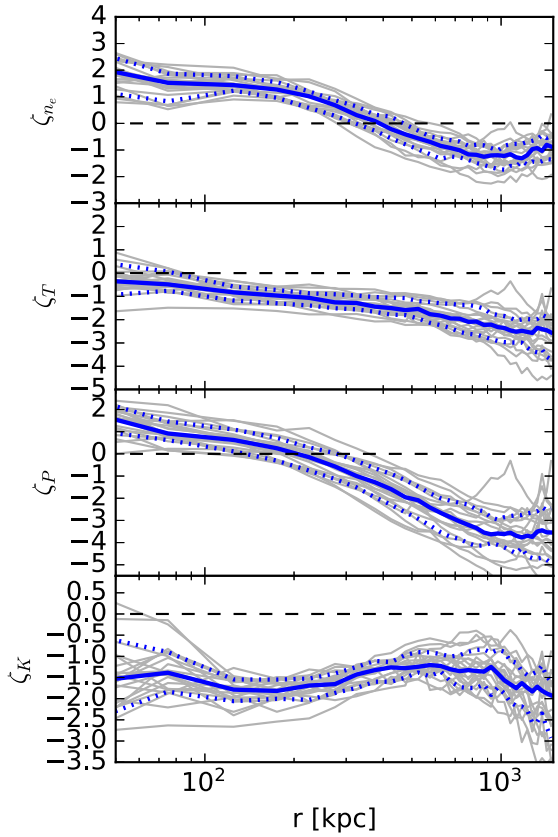

Figure 16. Radial profiles of the evolutionary rates of gas density (upper panel), Temperature (second panel from the top), Pressure (third panel from the top), and Entropy (bottom panel) of simulated clusters. The solid line indicates the mean profile, the dotted corridor the 68 per cent range, individual profiles are plotted in light grey. The horizontal dashed line marks the no-evolutionary case. Positive values indicates denser, hotter, higher pressure and entropy at high redshifts.

3.4 Comparison with literature

As discussed in the previous section, since clusters are not expanding (Peebles 1980; Figs 14 and 15) and with the purpose of comparing apples to apples, we did the comparison using unscaled units (kpc, keV cm^{-3}, etc) and we compared IDCS J1426.5+3508 profiles with those of present-day clusters 0.65 dex more massive. Given the large redshift baselines presently available, we propose that this choice is preferable to comparing clusters with the same mass M_{500}. For example, Bartalucci et al. (2017) low redshift sample is unlikely to be the descendant of their studied $z \sim 1$ sample and has actually lower mass if mass were measured inside the same physical aperture. Comparisons at fixed mass is compounding cluster evolution, dependence of profiles on cluster mass, and pseudo-evolution. The same problem holds using a mass enclosed in an overdensity anchored to the Universe matter density, such as with $M_{\Delta,m}$.

McDonald et al. (2017) computed the evolutionary rate of the electron density only, for lack of adequate data on other thermodynamic quantities, comparing a small $z \sim 1.4$ sample with lower redshift samples whose average mass increases with decreasing redshift in the attempt of comparing ancestors and descendants, as we also do. Similar to us, they used unscaled electron densities (see inset of their Fig. 3), but different from us, they measured the power of the $E(z)$ dependency using scaled radii, unlike our choice of using unscaled radii,

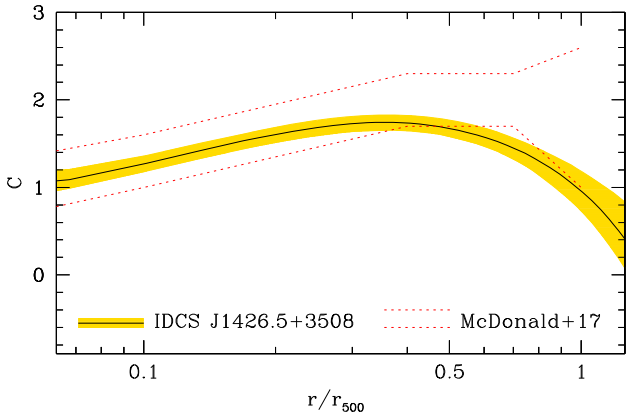

Figure 17. Electron density evolutionary rate C computed following McDonald et al. (2017). The evolution of the IDCS J1426.5+3508 electron density profile is indicated with the black line and yellow shading (mean value and 68 per cent uncertainties), and the McDonald et al. (2017) determination as the $\pm 1\sigma$ dotted corridor. The low value of C at $r \sim r_{500}$ indicates the need for a large gas density mass growth with this way of calculating the evolutionary rate.

$$n_e(r/r_{500,z}, z) = n_e(r/r_{500,z=0}, z = 0)E(z)^C \ . \quad (4)$$

This way of computing evolution complicates the interpretation of the results because an unique value of rate C takes different meanings at different radii: for example, a cluster with static profiles, such as the simulated haloes up to $r \approx r_{500,z=1.71}$, which therefore evolve at the same rate at all radii, would have $C = 0$ at the centre but $C \neq 0$ at r/r_{500} just because different r_{500} would be used at different z. Furthermore, the rate found at some radius r would differ from the one derived at a different radius r'. Therefore, we reiterate, the evolutionary rate derived using scaled radii C compounds evolution and pseudo-evolution.

Fig. 17 show the IDCS J1426.5+3508 electron density evolutionary rate computed following McDonald et al. (2017) using however X-COP in place of their $z = 0$ sample because the latter is not available in the needed form. The C value close to zero at large radii indicates that the IDCS J1426.5+3508 profile is dropping at those radii as their descendants do at much larger radii (at the same scaled radius r/r_{500}), not that the profile is unchanging here. Our and their electron density evolutionary rates agree (Fig. 17) at 1σ, although the authors interpret their uncertain C at large radius as $C = 2$, ruled out for IDCS J1426.5+3508 given its better S/N. These electron density rates complement each other: our rate uses a high S/N determination of one individual cluster at very high redshift, while their rate uses lower signal to noise data and is based on a sample, which should average out individual peculiar behaviours. Because of data limitations, the authors cannot address temperature, pressure, and entropy evolution.

Ghirardini et al. (2021) determine the evolutionary rate of seven clusters at $z_{\rm median} = 1.4$ mixing the two approaches above, making their choice completely orthogonal to ours. First, they used scaled radii, which compounds evolution and pseudo-evolution. Second, their comparison is at fixed mass, which compounds cluster evolution, dependence of profiles on cluster mass, and pseudo-evolution. In addition, the local cluster sample used is not representative at the considered (low for the present day) masses used in their comparison because their sample is selected against clusters of low pressure,

which exist in the mass range of their interest, such as CL2015 (Andreon et al. 2019).

The above differences between the ways evolution rates are computed have been overlooked in the past, which means that evolutionary claims should be reconsidered in light of the limitations of the used evolutionary rate definition. Agreement/disagreement among results of these authors should also be revisited adopting a common definition of evolutionary rate. Our proposed one, using unscaled profiles and radii at fixed ancestor, has the advantage of separating cluster evolution, dependence on mass, pseudo-evolution, and returns a number whose interpretation is the same at all radii.

4 CONCLUSIONS

We present well-resolved thermodynamic profiles out to 500 kpc (about r_{500}) of the $z = 1.75$ galaxy cluster IDCS J1426.5+3508. We combined intensity and spectral information from *Chandra* with an SZ map from MUSTANG-2. Thanks to this data set combination, IDCS J1426.5+3508 becomes the most distant cluster with resolved profiles, and also the high redshift cluster with most precise thermodynamic profiles. Profiles are distributed as supplementary material.

The profiles are derived using JOXSZ (Castagna & Andreon 2020) assuming a non-parametric pressure profile, to allow deviations from the universal pressure profile, and a very flexible model for the electron density profile. The analysis accounts for the instrument calibration uncertainties, background level systematics for both X-ray and SZ data, PSF and transfer function, and allows the X-ray temperature to differ from the SZ temperature, for example as a result of the known temperature systematics of Chandra.

The shape of the pressure profile, either derived from the SZ map alone or in conjunction with the X-ray data, turns out to be flatter than the universal pressure profile. Departures from the universal pressure profile, such as those observed for IDCS J1426.5+3508, show the risk of assuming an universal pressure profile when detecting clusters or measuring integrated pressure (often referred as 'mass'). Those may be responsible of the discrepancies found across instruments that are sensitive to different spatial scales.

The IDCS J1426.5+3508 temperature profile is radially increasing to r_{500} and the ICM presents an excess entropy compared to that expected in non-radiative simulations at large radii. We verified that these behaviours are robustly determined and derive from an electron density profile steeper than the pressure profile, both tightly constrained by the data.

The IDCS J1426.5+3508 local plausible descendants will be 0.65 ± 0.12 dex more massive according to our analysis of Multidark Planck 2 simulations. We therefore infer the evolution of ICM thermodynamics by comparing IDCS J1426.5+3508 to their massive descendants using unscaled radii and thermodynamic quantities. We identify three different radial regimes: in the very inner region, at 30 kpc, thermodynamic quantities have very similar values 10 Gyrs ago as today. Outside this region and within 300 kpc (about $r_{500}/2$), the gas is present in the right amount although cooler than in present-day clusters. Near 500 kpc (about r_{500}) IDCS J1426.5+3508 is short of gas, the gas present is too hot and has too much entropy, and the polytropic index is low. Therefore, heat and entropy should flow away from the region at 500 kpc and into smaller radii. This should happen with a large gas transfer at about 500 kpc to make the density profile shallower there, and little net gas transfer at smaller radii given the already appropriate electron density profile observed there. Non-thermal pressure, i.e. gas motion or turbulence, is also supported by the low polytropic index computed using the data, which are only sensitive to thermal pressure. The emerging picture is therefore one of a cluster in which a filamentary gas stream brings low entropy gas to r_{500} and energy to even smaller radii, which dissipates in form of heat, while 'central' values are unchanging, indicating a fine tuning between gas cooling and heating there.

To explore the possibly diverse evolution experienced by $z \sim 2$ clusters, observations of more high-redshift clusters are clearly needed. JKCS 041 at $z = 1.803$ (Andreon et al. 2009, 2014; Newman et al. 2014) is just being observed and will be reported soon.

In this work, we also introduce a new definition of the evolutionary rate that uses unscaled radii and thermodymamic quantities at fixed progenitor, i.e. which compares clusters of different masses at different redshifts in order to compar ancestors with descendants. It has the advantage of separating cluster evolution, dependence on mass, pseudo-evolution, and returns a number with a unique interpretation, unlike definitions used in literature. Finally, we show that a 100 ks *Chandra* exposure and a regular MUSTANG-2 observation compete favourably against a longer *Chandra* exposure and an XMM observation of exceptional duration in the determination of thermodynamic profiles.

ACKNOWLEDGEMENTS

FC acknowledges financial contribution from the agreement ASI-INAF n.2017-14-H.0 and PRIN MIUR 2015 Cosmology and Fundamental Physics: Illuminating the Dark Universe with Euclid. The Green Bank Observatory is a facility of the National Science Foundation operated under cooperative agreement by Associated Universities, Inc. MUSTANG-2, on the GBT, data was taken under the project ID AGBT18A_336. The CosmoSim database used in this paper is a service by the Leibniz-Institute for Astrophysics Potsdam (AIP) and SA thanks Harry Enke for suggestions about its use. The MultiDark database was developed in cooperation with the Spanish MultiDark Consolider Project CSD2009-00064.

DATA AVAILABILITY

Raw Chandra data are public available in the Chandra archive, obs ID 15168 and 16321. SZ derived products (beam, transfer function, and map) are available at https://doi.org/10.7910/DVN/Q1QMQS. Radial thermodynamic profiles are distributed as supplement material and at the URL above.

REFERENCES

AMI Consortium et al., 2013, MNRAS, 433, 2920
Andreon S., 2010, MNRAS, 407, 263
Andreon S., Bergé J., 2012, A&A, 547, A117
Andreon S., Ettori S., 1999, ApJ, 516, 647
Andreon S. et al., 2008, MNRAS, 383, 102
Andreon S. et al., 2009, A&A, 507, 147
Andreon S. et al., 2014, A&A, 565, A120
Andreon S. et al., 2019, A&A, 630, A78
Arnaud M., et al., 2010, A&A, 517, A92
Bartalucci I. et al., 2018, A&A, 617, A64
Behroozi P. S., Wechsler R. H., Wu H.-Y., 2013, ApJ, 762, 109
Böhringer H., Dolag K., Chon G., 2012, A&A, 539, A120
Botteon A., Gastaldello F., Brunetti G., 2018, MNRAS, 476, 5591
Borgani S. et al., 2004, MNRAS, 348, 1078
Brodwin M. et al., 2012, ApJ, 753, 162
Brodwin M. et al., 2015, ApJ, 806, 26
Brodwin M. et al., 2016, ApJ, 817, 122

Castagna F., Andreon S., 2019, A&A, 632, A22
Castagna F., Andreon S., 2020, A&A, 639, A73
Dicker S. R. et al., 2014, Proc. SPIE, 91530J
Dicker S. R. et al., 2020, ApJ, 902, 144
Di Mascolo L. et al., 2019, A&A, 628, A100
Di Mascolo L. et al., 2020, A&A, 638, A70
Dolag K. 2016, MNRAS, 463, 1797
Fomalont E. et al., 2014, Messenger, 155, 19
Fruscione A. et al., 2006, Proc. SPIE, 62701V
Garmire G. P. et al., 2003, Proc. SPIE, 4851, 28
Ghirardini V. et al., 2019, A&A, 621, A41
Ghirardini V. et al., 2021, ApJ, 910, 14
Ginsburg A. et al., 2020, ApJS, 248, 24
Gott J. R., Rees M. J., 1975, A&A, 45, 365
Gunn J. E., 1977, ApJ, 218, 592.
Hilton M. et al., 2018, ApJS, 235, 20
Hirschmann M. et al., 2014, MNRAS, 442, 2304
Kalberla P. M. W. et al., 2005, A&A, 440, 775
Kitayama T. et al., 2004, PASJ, 56, 17
Klypin A. et al., 2016, MNRAS, 457, 4340
Korngut P. M. et al., 2011, ApJ, 734, 10
Kravtsov A. V., Borgani S., 2012, ARA&A, 50, 353
Iguchi S. et al., 2009, PASJ, 61, 1
Lu Y. et al., 2006, MNRAS, 368, 1931
McDonald M. et al., 2014, ApJ, 794, 67
McDonald M. et al., 2017, ApJ, 843, 28
Mantz A. B. et al., 2014, ApJ, 794, 157
Mantz A. B. et al., 2018, A&A, 620, A2
Mason B. S. et al., 2010, ApJ, 716, 739
Mroczkowski T. et al., 2019, Space Sci. Rev., 215, 17
Navarro J. F., Frenk C. S., White S. D. M., 1997, ApJ, 490, 493
Owers M. S. et al., 2014, ApJ, 780, 163
Peebles P. J. E., 1980, Large-scale Structure of the Universe. Princeton University Press Princeton, NJ
Planck Collaboration, 2014, A&A, 571, A29
Pratt G. W. et al., 2010, A&A, 511, A85
Ragagnin A. et al., 2017, Astron. Comput., 20, 52
Romero C. E. et al., 2020, ApJ, 891, 90
Rossetti M. et al., 2013, A&A, 556, A44
Rumsey C. et al., 2016, MNRAS, 460, 569
Sanders J. S. et al., 2018, MNRAS, 474, 1065
Shaw L. D. et al., 2010, ApJ, 725, 1452
Simionescu A. et al., 2012, ApJ, 757, 182
Sonkamble S. S. et al., 2015, Ap&SS, 359, 21
Stanford S. A. et al., 2012, ApJ, 753, 164
Strüder L. et al., 2001, A&A, 365, L18
Sunyaev R. A., Zeldovich Y. B., 1972, A&A, 20, 189
Turner M. J. L. et al., 2001, A&A, 365, L27
van Kempen T. et al., 2014, ALMA Memo, 598
Vikhlinin A. et al., 2006, ApJ, 640, 691
Voit G. M., Kay S. T., Bryan G. L., 2005, MNRAS, 364, 909
Zhao D. H. et al., 2003, MNRAS, 339, 12

SUPPORTING INFORMATION

Supplementary data are available at *MNRAS* online.

suppl_data

Please note: Oxford University Press is not responsible for the content or functionality of any supporting materials supplied by the authors. Any queries (other than missing material) should be directed to the corresponding author for the article.

This paper has been typeset from a TEX/LATEX file prepared by the author.